Backward electroproduction of π^0 mesons on protons in the region of nucleon resonances at four momentum transfer squared $Q^2 = 1.0GeV^2$

G. Laveissiere, N. Degrande, S. Jaminion, C. Jutier, L. Todor, R. Di Salvo, L. van Hoorebeke, L.C. Alexa Stony, B.D. Anderson, K.A. Aniol, et al.

Backward electroproduction of π^0 mesons on protons in the region of nucleon resonances at four momentum transfer squared $Q^2 = 1.0$ GeV^2

G. Laveissière,[1] N. Degrande,[2] S. Jaminion,[1] C. Jutier,[1,3] L. Todor,[3] R. Di Salvo,[1] L. Van Hoorebeke,[2] L.C. Alexa,[4] B.D. Anderson,[5] K.A. Aniol,[6] K. Arundell,[7] G. Audit,[8] L. Auerbach,[9] F.T. Baker,[10] M. Baylac,[8] J. Berthot,[1] P.Y. Bertin,[1] W. Bertozzi,[11] L. Bimbot,[12] W.U. Boeglin,[13] E.J. Brash,[4] V. Breton,[1] H. Breuer,[14] E. Burtin,[8] J.R. Calarco,[15] L.S. Cardman,[16] C. Cavata,[8] C.-C. Chang,[14] J.-P. Chen,[16] E. Chudakov,[16] E. Cisbani,[17] D.S. Dale,[18] C.W. De Jager,[16] R. De Leo,[19] A. Deur,[1] N. d'Hose,[8] G.E. Dodge,[3] J.J. Domingo,[16] L. Elouadrhiri,[16] M.B. Epstein,[6] L.A. Ewell,[14] J.M. Finn,[7] K.G. Fissum,[11] H. Fonvieille,[1] G. Fournier,[8] B. Frois,[8] S. Frullani,[17] C. Furget,[20] H. Gao,[11] J. Gao,[11] F. Garibaldi,[17] A. Gasparian,[21,18] S. Gilad,[11] R. Gilman,[22,16] A. Glamazdin,[23] C. Glashausser,[22] J. Gomez,[16] V. Gorbenko,[23] P. Grenier,[1] P.A.M. Guichon,[8] J.O. Hansen,[16] R. Holmes,[24] M. Holtrop,[15] C. Howell,[25] G.M. Huber,[4] C.E. Hyde-Wright,[3] S. Incerti,[9] M. Iodice,[17] J. Jardillier,[8] M.K. Jones,[7] W. Kahl,[24] S. Kamalov,[26] S. Kato,[27] A.T. Katramatou,[5] J.J. Kelly,[14] S. Kerhoas,[8] A. Ketikyan,[28] M. Khayat,[5] K. Kino,[29] S. Kox,[20] L.H. Kramer,[13] K.S. Kumar,[30] G. Kumbartzki,[22] M. Kuss,[16] A. Leone,[31] J.J. LeRose,[16] M. Liang,[16] R.A. Lindgren,[32] N. Liyanage,[11] G.J. Lolos,[4] R.W. Lourie,[33] R. Madey,[5] K. Maeda,[29] S. Malov,[22] D.M. Manley,[5] C. Marchand,[8] D. Marchand,[8] D.J. Margaziotis,[6] P. Markowitz,[13] J. Marroncle,[8] J. Martino,[8] C.J. Martoff,[9] K. McCormick,[3] J. McIntyre,[22] S. Mehrabyan,[28] F. Merchez,[20] Z.E. Meziani,[9] R. Michaels,[16] G.W. Miller,[30] J.Y. Mougey,[20] S.K. Nanda,[16] D. Neyret,[8] E.A.J.M. Offermann,[16] Z. Papandreou,[4] C.F. Perdrisat,[7] R. Perrino,[31] G.G. Petratos,[5] S. Platchkov,[8] R. Pomatsalyuk,[23] D.L. Prout,[5] V.A. Punjabi,[34] T. Pussieux,[8] G. Quémenér,[1,7] R.D. Ransome,[22] O. Ravel,[1] J.S. Real,[20] F. Renard,[8] Y. Roblin,[1] D. Rowntree,[11] G. Rutledge,[7] P.M. Rutt,[22] A. Saha,[16] T. Saito,[29] A.J. Sarty,[35] A. Serdarevic,[4,16] T. Smith,[15] G. Smirnov,[1] K. Soldi,[36] P. Sorokin,[23] P.A. Souder,[24] R. Suleiman,[11] J.A. Templon,[10] T. Terasawa,[29] L. Tiator,[26] R. Tieulent,[20] E. Tomasi-Gustaffson,[8] H. Tsubota,[29] H. Ueno,[27] P.E. Ulmer,[3] G.M. Urciuoli,[17] R. Van De Vyver,[2] R.L.J. Van der Meer,[4] P. Vernin,[8] B. Vlahovic,[36] H. Voskanyan,[28] E. Voutier,[20] J.W. Watson,[5] L.B. Weinstein,[3] K. Wijesooriya,[7] R. Wilson,[37] B.B. Wojtsekhowski,[16] D.G. Zainea,[4] W-M. Zhang,[5] J. Zhao,[11] and Z.-L. Zhou[11]

(The Jefferson Lab Hall A Collaboration)

[1] *Université Blaise Pascal/IN2P3, F-63177 Aubière, France*
[2] *University of Gent, B-9000 Gent, Belgium*
[3] *Old Dominion University, Norfolk, VA 23529*
[4] *University of Regina, Regina, SK S4S OA2, Canada*
[5] *Kent State University, Kent OH 44242*
[6] *California State University, Los Angeles, CA 90032*
[7] *College of William and Mary, Williamsburg, VA 23187*
[8] *CEA Saclay, F-91191 Gif-sur-Yvette, France*
[9] *Temple University, Philadelphia, PA 19122*
[10] *University of Georgia, Athens, GA 30602*
[11] *Massachusetts Institute of Technology, Cambridge, MA 02139*
[12] *Institut de Physique Nucléaire, F-91406 Orsay, France*
[13] *Florida International University, Miami, FL 33199*
[14] *University of Maryland, College Park, MD 20742*
[15] *University of New Hampshire, Durham, NH 03824*
[16] *Thomas Jefferson National Accelerator Facility, Newport News, VA 23606*
[17] *INFN, Sezione Sanità and Istituto Superiore di Sanità, 00161 Rome, Italy*
[18] *University of Kentucky, Lexington, KY 40506*
[19] *INFN, Sezione di Bari and University of Bari, 70126 Bari, Italy*
[20] *Laboratoire de Physique Subatomique et de Cosmologie, F-38026 Grenoble, France*
[21] *Hampton University, Hampton, VA 23668*
[22] *Rutgers, The State University of New Jersey, Piscataway, NJ 08855*
[23] *Kharkov Institute of Physics and Technology, Kharkov 61108, Ukraine*
[24] *Syracuse University, Syracuse, NY 13244*
[25] *Duke University, Durham, NC 27706*
[26] *Institut fuer Kernphysik, University of Mainz, D-55099 Mainz, Germany*
[27] *Yamagata University, Yamagata 990, Japan*
[28] *Yerevan Physics Institute, Yerevan 375036, Armenia*
[29] *Tohoku University, Sendai 980, Japan*
[30] *Princeton University, Princeton, NJ 08544*
[31] *INFN, Sezione di Lecce, 73100 Lecce, Italy*
[32] *University of Virginia, Charlottesville, VA 22901*

[33] *State University of New York at Stony Brook, Stony Brook, NY 11794*
[34] *Norfolk State University, Norfolk, VA 23504*
[35] *Florida State University, Tallahassee, FL 32306*
[36] *North Carolina Central University, Durham, NC 27707*
[37] *Harvard University, Cambridge, MA 02138*

Backward exclusive electroproduction of π^0 mesons on protons has been measured at $Q^2 = 1.0$ GeV^2 by detecting protons in the forward direction in coincidence with scattered electrons from the 4 GeV electron beam in Jefferson Lab's Hall A. The data span the range of the total $(\gamma^* p)$ center-of-mass energy W from the pion production threshold to $W = 2.0$ GeV. The azimuthally separated differential cross sections $\sigma_{\rm T} + \epsilon\ \sigma_{\rm L}$, $\sigma_{\rm TL}$, and $\sigma_{\rm TT}$ from this experiment are presented together with the MAID2000 [10] and SAID [11, 12] parametrizations.

PACS numbers: 23.23.+x,56.65.Dy

I. INTRODUCTION

The present experiment [1] exploits the attractive opportunity to investigate a number of resonance states by detecting their decay into two channels of very similar kinematics, but remarkably different final state interaction (FSI) couplings. They are:

$$e^- + p \rightarrow e^- + p + \pi^0 \tag{1}$$

and

$$e^- + p \rightarrow e^- + p + \gamma. \tag{2}$$

The intermediate resonant state decays via the strong interaction in reaction (1), and via the electromagnetic interaction in reaction (2). However one can employ an identical technique for detecting two of the three outgoing particles for both reactions, namely detection of the scattered electron and proton in coincidence. This results in a greater precision for the relative cross sections of the two reactions than for either cross sections alone.

A comparison of reactions (1) and (2) may be beneficial in addressing the problem of the "missing" resonances. The Constituent Quark Model (CQM) [2] predicts several positive parity states at $W > 1.6$ GeV that have not been seen experimentally [3, 4, 5, 6, 7]. It is conjectured that these states couple relatively weakly to the πN channel which has dominated (either in the initial or final state) most of the experimental work to date. The two reactions (1) and (2) provide therefore a contrast in potentially very different sensitivity to the missing resonances.

Closely related to reactions (1) and (2) is the process of deep inelastic electron scattering, which is generally analysed in terms of parton rather than baryon resonance degrees of freedom. However, the phenomenology of quark-hadron duality illustrates the interplay of these two frameworks at modest Q^2 and W [8, 9]. Another motivation for the present study is to explore the exclusive reactions (1) and (2) in the high energy limit, where current quark degrees of freedom may play as important a role as resonance, or constituent quark, degrees of freedom.

In the absence of a theoretical approach based on fundamental principles, one has to rely on experimental input and use phenomenological models. In the region of the first resonance, $\Delta(1232)$, many models are in a well developed stage and are successful in describing the resonance spectrum quantitatively: MAID [10], SAID [11, 12], etc [13, 14, 15]. One finds a substantial increase in uncertainties for masses and hadronic and electromagnetic couplings of higher resonances where competition between resonant and non-resonant channels rises. An increase in the total center-of-mass (cm) energy W is followed by an increase in the number of coupled channels, which have to be related via unitarity. At this point, even the use of all available data on the resonance production cannot resolve the difficulties of the model approaches in particular for $W > 1.6$ GeV. To constrain these hadronic and EM couplings, there is currently an intensive world-wide effort to simultaneously study all the decay channels produced in photo- and electromagnetic excitation of the nucleon [16].

Reaction (2) will be presented in a future paper. In this paper we present cross section measurements of reaction (1) made in Hall A of the Thomas Jefferson National Accelerator Facility (JLab) at an incident electron energy 4 GeV and fixed four-momentum transfer squared $Q^2 = 1.0$ GeV^2. The scattered electron and proton, momentum k' and p' respectively, are detected at laboratory angles θ_e and θ_p, and the neutral pion is reconstructed using a missing mass technique. The missing mass squared is expressed as $M_X^2 = (k + p - k' - p')^2$ where k and p are the momentum of the initial electron and proton respectively. The relevant kinematical variables are shown in Fig. 1.

The kinematics were further restricted to forward detection (relative to the virtual photon momentum vector) of the recoil proton (backward center of mass π^0 emission). This reaction has been studied previously at the NINA electron synchrotron at a beam energy 4 GeV [17], at DESY at 2.7 and 3.2 GeV [18, 19, 20, 21] and, recently, in Hall C [22] and Hall B[23] experiments at JLab.

Our results will be presented as conventional center of mass photo-production cross sections, where the photon flux factor (Hand convention) is introduced in the one-

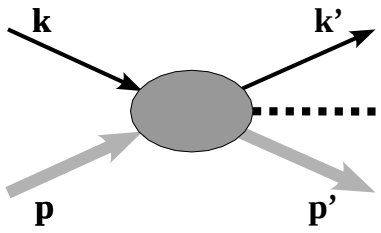

FIG. 1: Definition of kinematic variables for reaction (1). Thin lines represent the incident and outgoing electrons, and thick lines correspond to the target and recoil protons. The dashed line stands for the produced neutral pion.

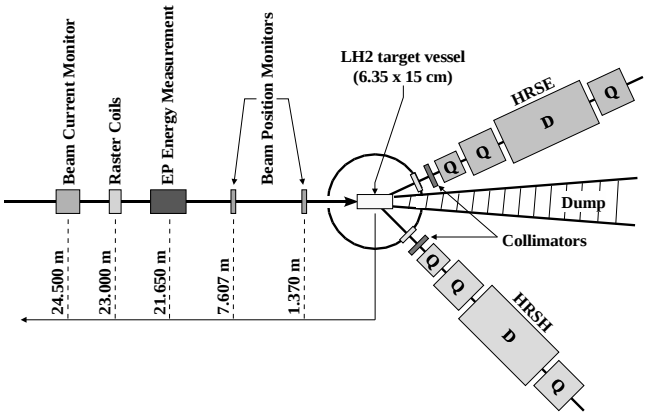

FIG. 2: Layout of the Hall A experimental setup.

photon-exchange approximation:

$$\frac{d^5\sigma}{dk' d\Omega_{k'} d\Omega^*_\pi} = \Gamma \, \frac{d^2\sigma}{d\Omega^*_\pi}, \tag{3}$$

$$\Gamma = \frac{\alpha}{2\pi^2} \, \frac{k'}{k} \, \frac{W^2 - \mathrm{M}_p^2}{2\mathrm{M}_p \cdot Q^2} \, \frac{1}{1-\epsilon}, \tag{4}$$

where ϵ is the virtual photon polarization:

$$\epsilon = \frac{1}{1 + 2\frac{(\vec{k}-\vec{k'})^2}{Q^2} tan^2(\frac{\theta_e}{2})}. \tag{5}$$

In the following, θ^* is defined as the polar angle between the virtual photon and the pion (missing particle) in the pion-proton center of mass system. ϕ is the azimuthal angle between the leptonic and the hadronic planes (ϕ is taken equal to 0 when the missing particle is emitted in the half plane containing the outgoing electron). This two-fold differential cross section is developed as a function of transverse, longitudinal and interference parts $d^2\sigma_{\mathrm{T}}$, $d^2\sigma_{\mathrm{L}}$, $d^2\sigma_{\mathrm{TL}}$ and $d^2\sigma_{\mathrm{TT}}$, that only depend on W, Q^2 and θ^* :

$$\begin{aligned}\frac{d^2\sigma}{d\Omega^*_\pi} \;=\; & \frac{d^2\sigma_{\mathrm{T}}}{d\Omega^*_\pi} \;+\; \epsilon \, \frac{d^2\sigma_{\mathrm{L}}}{d\Omega^*_\pi} + \sqrt{2\epsilon(1+\epsilon)} \, \frac{d^2\sigma_{\mathrm{TL}}}{d\Omega^*_\pi} \cos\phi \\ & + \epsilon \, \frac{d^2\sigma_{\mathrm{TT}}}{d\Omega^*_\pi} \cos 2\phi. \end{aligned} \tag{6}$$

In the rest of the paper, we will refer to the differential cross sections as $\sigma_{\mathrm{T}} + \epsilon \, \sigma_{\mathrm{L}}$, σ_{TL} and σ_{TT}.

II. EXPERIMENTAL PROCEDURE AND DATA ANALYSIS

A. Apparatus

The experiment was performed using the continuous electron beam with an energy of 4032 MeV incident on a liquid hydrogen target. The scattered electron and the recoil proton are detected in coincidence in two high resolution spectrometers (HRSE and HRSH). Fig. 2 is a top view of the experimental set-up and the relevant components. More information on the Hall A setup will be available in [24].

1. Electron beam

Typical beam intensities ranged from 60 to 120 μA; they were continuously monitored during data taking using two resonant cavity beam current monitors (BCM) [25]. An absolute calibration of the BCM was performed at least once per day by employing an Unser transformer [26]. The measured standard deviation and drift of the BCM ensured a stability of the current measurement of ± 0.3 % over the entire experiment. In order to avoid local boiling of hydrogen in the target, the incident beam was rastered (± 4 mm horiz. and vert.) with the use of two asynchronized horizontal and vertical magnetic coils ($\approx$ 20 kHz) located 23 m upstream of the target. The instantaneous position of the beam at the target was determined with an accuracy of about 100 μm with a pair of beam position monitors (BPM) located at 7.607 m and 1.370 m upstream of the target [27]. Each BPM is a resonant cavity with a set of four antenna wires parallel to the beam axis. The difference between the signals on opposing wires is proportional to the beam position. The raster amplitude was calibrated with a thin tungsten wire (harp scanner) moved through the beam path, thus defining the beam spot size.

2. Target

The liquid hydrogen (LH_2) target material was contained in a cylindrical aluminium vessel (0.0635 m diameter and 0.15 m long along the beam axis - see Fig. 2). The target wall thickness was 175 μm. The entrance and

exit windows were 71 and 94 μm thick, respectively [28].

The target itself is located inside a cylindrical aluminum scattering chamber connected to the beamline vacuum. The scattering chamber was equipped with two 400 μm aluminium exit windows, each facing a spectrometer.

The working temperature and pressure of the hydrogen loop (19.0 K and 25 psia) give a nominal density ρ_0 of 0.0723 g/cm^3.

The data taken within 100 s after each substantial beam intensity variation (e.g. beam trips) were excluded from the analysis to avoid instabilities in the target density.

3. Magnetic spectrometers

The two high resolution spectrometers (HRS) of QQDQ type are of identical conception. Their main characteristics include a central momentum range from 0.3 to 4.0 GeV/c, and nominal acceptance of $\pm$ 4.5% in momentum, $\pm$ 65 mrad in vertical angle, $\pm$ 30 mrad in horizontal angle, and $\pm$ 5 cm in target length (transverse to the spectrometer axis). The magnetic dipole in each spectrometer deflects the particle trajectories in the vertical plane by 45° over a 2 m long focal plane. The acceptance is defined in part by a tungsten collimator positioned at 1.109 m and 1.100 m (respectively for the electron and hadron arms) from the target, and by the apertures of the magnets. The vacuum box of the spectrometer is closed by a 178 μm Kapton entrance window and a 100 μm titanium exit window. In this experiment, the spectrometers were positioned with an absolute angular accuracy of 0.5 mrad.

4. Detectors

The detector package of each spectrometer is shown in Fig. 3. It includes:

- Two vertical drift chambers (VDC) [29], spaced by 50 cm, to define the trajectories of the charged particles; each VDC is equipped with two wire planes, to measure the intercepts and slopes of each trajectory in two perpendicular planes; charged particles passing within the acceptance of the spectrometer cross the plane of the chambers hitting from 3 to 5 sense wires. Each sense wire starts an updating time to digital converter (TDC) which is stopped by the acquisition trigger.

- Two scintillator planes S_1 and S_2 each consisting of 6 plastic scintillator paddles. The S_1 paddles are 29.3 cm (dispersive) by 36.0 cm (transverse) and the S_2 paddles are 37.0 cm (dispersive) by 60.0 cm (transverse). In both planes the paddles overlap by 0.5 cm. Each paddle is viewed by 2 photomultiplier tubes (PMT) at opposite ends.

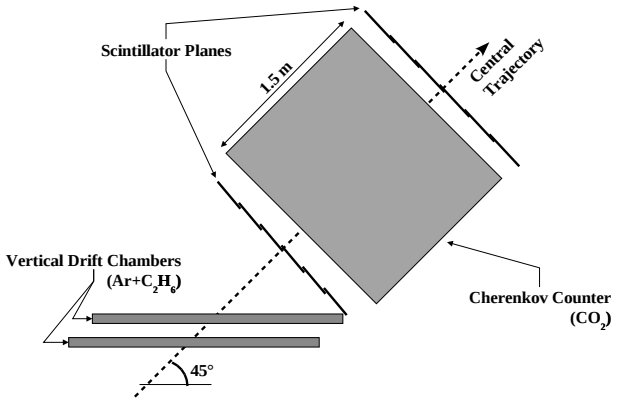

FIG. 3: HRSE detector package. The vertical drift chambers as well as the trigger scintillator hodoscopes are common to both spectrometers.

- A gas Cherenkov counter (filled with CO_2) viewed by 10 PMT's. Only the Cherenkov counter of the electron spectrometer was used in this experiment.

Each PMT output is fed to an amplitude to digital converter (charge integrating ADC) and to a discriminator. Each discriminator signal is sent to a time to digital converter (TDC) and to the fast electronics logic.

5. Trigger electronics and data acquisition

Fast electronics logic defines several trigger signals for the data acquisition system (DAQ) using CEBAF Online Data Acquisition (CODA v1.4) [30]:

- T1 (T3) corresponds to a good electron (proton) event. It requires a coincidence between a paddle i of the S_1 plane and a paddle j of the S_2 plane within the directivity limits of the spectrometer ($|i-j| \leq 1$). Each paddle event (S_1 or S_2) requires a coincidence between the two PMT's at the ends of the paddle.

- T2 (T4) defines a deficient electron (proton) event. This requires that either the $S_1 \cap S_2$ coincidence is not within the directivity limits ($|i-j| > 1$) or that only one scintillator plane fires. For the T2 trigger, if only one scintillator plane has a two ended coincidence, the trigger logic requires a coincidence with the gas Cherenkov counter signal.

- T5 is the main trigger and is defined by a coincidence of T1 and T3 within 100 ns.

Although all triggers can fire the DAQ, T5 has priority while other triggers are prescaled. This fraction is set using prescale factors (PS_1, PS_2, PS_3 and PS_4). The encoding of the analog signals and the transfer of the digitized signal to the computer buffers takes $\sim$ 700 μs.

When the DAQ is triggered, it forbids any other trigger until the first is processed. This induces acquisition dead times up to 30 % for some high counting rate conditions. The number of events for every trigger type is recorded by a running scaler, which is read and logged by the DAQ every 10 seconds.

B. Data taking geometry

Data were taken at nine spectrometer angle and momentum settings (numbers 4-12 in Table I), covering the entire resonance region, i.e. a total cm energy W varying between pion threshold and 2.0 GeV. W is the invariant mass of the $(\gamma^* p)$ system, $W = \sqrt{(k - k' + p)^2}$. The acceptance in θ^* was centered around 180°. Complementary measurements (settings #1, 2, 3 in Table I) were included in order to increase the statistical accuracy around the pion production threshold. Additional $H(e,e')p$ elastic scattering measurements with a sieve slit (and both spectrometers tuned to electrons) and Al, $C(e,e')X$ quasi-elastic measurements with an array of foil targets served for calibration of detectors and spectrometer optics. The relevant information on production data is summarized in Table I.

TABLE I: Kinematical settings used for the π^0 data taking. The incident electron energy was 4032 MeV (discussed in Section II C 1). The values shown in the table are the central values within the acceptance.

Setting number	W_{nom} (GeV)	k'_{nom} (GeV/c)	$(\theta_e)_{nom}$ (°)	p'_{nom} (GeV/c)	$(\theta_p)_{nom}$ (°)
1	1.180	3.433	15.43	1.187	-50.00
2	1.178	3.433	15.43	1.187	-48.50
3	1.177	3.433	15.43	1.187	-46.50
4	1.217	3.282	15.77	1.323	-45.41
5	1.252	3.176	16.04	1.418	-41.67
6	1.326	3.043	16.39	1.539	-37.49
7	1.431	2.909	16.76	1.662	-33.82
8	1.526	2.776	17.16	1.787	-30.60
9	1.613	2.642	17.87	1.914	-27.75
10	1.690	2.482	18.15	2.067	-24.75
11	1.795	2.269	18.99	2.274	-21.34
12	1.894	2.056	19.96	2.482	-18.46

C. Data analysis

1. Method

The data analysis procedure includes several passes. In a first step, the selection of the CODA event is performed by rejecting any sequence collected when one of the stability requirements fails: beam intensity or position, spectrometer magnetic elements, etc.

Next, the Hall A analyzer ESPACE (Event Scanning Program for Hall A Collaboration Experiments) [31] is used to build the trajectory of the particles in the spectrometer focal plane from the VDCs data : two position coordinates $X_{\rm fp}$ and $Y_{\rm fp}$ and two cartesian angles $\phi_{\rm fp}$ and $\theta_{\rm fp}$.

Then, using the beam position information at the target and the database for the spectrometers optics, ESPACE reconstructs the entire kinematics of the electron and the proton at vertex, as well as the interaction point. This database has been optimized for the kinematical settings of this experiment [32]. Both particles at the vertex are described with four spectrometer variables : the transverse coordinate $Y_{\rm tg}$, the two cartesian angles $\phi_{\rm tg}$ and $\theta_{\rm tg}$, and the relative momentum

$$\delta k' = \frac{k' - k'_{\rm nom}}{k'_{\rm nom}} \text{ (electron)} \quad (7)$$

$$\delta p' = \frac{p' - p'_{\rm nom}}{p'_{\rm nom}} \text{ (proton).} \quad (8)$$

The dispersive coordinate $X_{\rm tg}$ is deduced from the beam information. The energy losses in the target and spectrometer windows are also taken into account.

At this stage, the position and the shape of the missing mass squared M_X^2 distribution are indicators of how the positioning of the spectrometers and the beam are under control. A minimization of the missing mass is done in order to obtain a fine tune of the beam energy, of the vertical angle $\theta_{\rm tg}$ of the electron arm, of the horizontal angles of both arms $\phi_{\rm tg}$, and of the vertical beam raster amplitude at the target. The result of this minimization for the beam energy yields an average correction of -13 MeV to the nominal value of 4045 MeV, with a dispersion of $\pm$ 3 MeV, varying from one run to another. A similar procedure based on the horizontal position of the reconstructed vertex is used to determine the horizontal raster amplitude of the beam and the horizontal mispointing of the spectrometers.

2. Simulation and radiative corrections

We use a detailed simulation [33] which takes into account all processes that affect the characteristics of the experimental data. Indeed, these data stem from a convolution of the "ideal" events defined at the vertex with a number of processes that influence the incident beam and the outgoing (detected) particles. The simulation incorporates the beam profile distribution, collisional energy losses, multiple scattering, internal and external bremsstrahlung and radiative corrections [34], as well as other resolution effects (*e.g.* from optics and detector resolution). The spectrometers acceptance is simulated with a model based on the optic design of the spectrometer and field maps of the magnets [32]. Events are generated according to a model cross section $d\sigma_{\rm model}$. In a first step, $d\sigma_{\rm model}$=MAID2000 [10] (this is discussed in Section III). In a second step we add a dependence on Q^2 based on our experimental results (Section IV).

In order to reconcile the results of simulation with the data, an additional smearing had to be combined with the simulated resolution effects. The corrections depend on the data taking geometry and are listed in Table II.

TABLE II: Additional Gaussian resolution smearing at each experimental setting (rms) for reconstructed variables at target.

	electron			proton		
Setting number	$\theta_{\rm tg}$ (mrad)	$Y_{\rm tg}$ (mm)	$\delta p'$ (10^{-4})	$\phi_{\rm tg}$ (mrad)	$\theta_{\rm tg}$ (mrad)	$Y_{\rm tg}$ (mm)
1	1.00	.00	2.00	1.00	2.00	.30
2	1.00	.00	2.00	1.00	2.00	.30
3	1.00	.00	2.00	1.00	2.00	.30
4	1.35	.30	2.75	1.35	2.75	.30
5	1.45	.42	3.00	1.45	3.00	.42
6	1.80	.33	3.60	1.80	3.60	.33
7	1.65	.00	3.30	1.65	3.30	.00
8	1.80	.66	3.60	1.80	3.60	.66
9	1.80	.66	3.60	1.80	3.60	.66
10	1.80	.66	3.60	1.80	3.60	.66
11	1.80	.66	3.60	1.80	3.60	.66
12	1.50	.66	3.00	1.50	3.00	.66

Our procedure for radiative corrections has been actually developed for process (2) following the exponentiation method of [34], and has been applied in the same way to process (1).

In this method, radiative corrections are implemented in two parts according to the source of photon radiation. The first contribution is the acceptance-dependent part of the internal and external bremsstrahlung from the electron lines, and as such it is included in the simulation [33]. This reproduces the radiative tail in the missing mass squared spectrum (see Fig. 5). The second contribution is expressed as a constant factor equal to 0.93 at $Q^2 = 1.0$ GeV^2 applied to the cross section. The systematic error associated with the radiative corrections is taken equal to $\pm 2\%$ [34].

3. π^0 event selection

The following criteria and cuts have been applied to properly select the π^0 events :

- A suitable coincidence timing window, as illustrated in Fig. 4.
- A directivity cut applied on the particle's position in the collimator plane at the entrance of each spectrometer : ± 2.9 cm in horizontal and ± 5.8 cm in vertical (This corresponds to 87% of the total geometrical acceptance of the 6 msr collimator).
- An acceptance cut defined for both arms by :

$$\delta k'(p') \leq A \pm B * \phi_{\rm tg} + C * Y_{\rm tg}^2 \qquad (9)$$

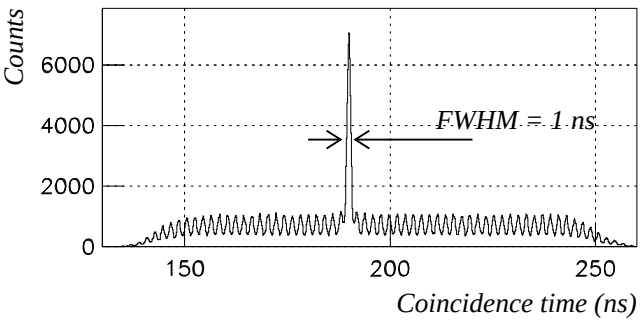

FIG. 4: Coincidence time for setting #7. The time is corrected for the path length in the spectrometer and for the proton velocity. The fine structure in the time spectrum is due to the 500 MHz structure of the beam.

with $A = 0.17$, $B = 6.0$ rad^{-1} and $C = -23.15$ m^{-2}. This cut approximates the dipole aperture and was used to symmetrise the acceptance which is not completely defined by the collimator alone.

- An acceptance cut defined in both arms in the plane $(Y_{\rm tg}, \phi_{\rm tg})$. This cut has a diamond hexagonal shape and tends to reproduce the quadrupoles apertures. More information on this cut is given in [36].
- A cut on the horizontal transverse distance d between the beam and the reconstructed vertex (using both arms) :

$$|d| < 0.003 \text{ m} \qquad (10)$$

- A selection window on the missing mass squared : $10000 < M_x^2 < 50000$ MeV^2. The lower boundary of the selection window serves to suppress the yield from reaction (2) which is manifested as a peak at $M_X^2 = 0$ in Fig. 5.

D. Cross sections evaluation

1. Extraction method

In the present analysis, a typical experimental bin of phase space is defined in the five kinematic variables Q^2, W, ϵ, $\cos\theta^*$, ϕ, and the missing mass squared M_X^2. The number of events in each bin is the product of the integrated luminosity $\mathcal{L}$ and the convolution of the physical cross section with resolution effects over all the experimental acceptance. Let N_i denote the number of counts observed in bin i, and $\mathcal{K}_i$ the experimental resolution and acceptance function of the same bin. Then

$$N_i = \mathcal{L} \int \left[d^6\sigma \otimes \mathcal{K}_i \right]. \qquad (11)$$

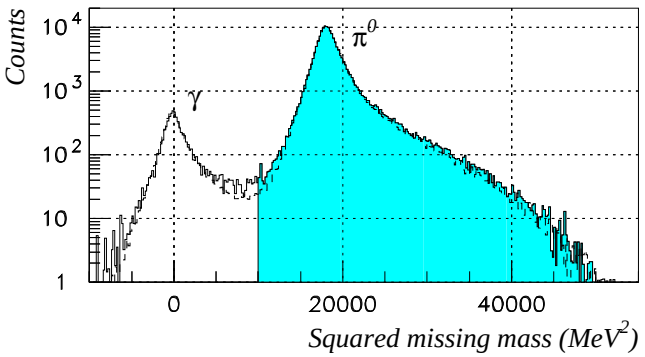

FIG. 5: Experimental distribution of the missing mass squared (solid) and the corresponding simulated spectrum (dashed line) obtained by registering the process p(e,e'p)X. The peak around zero corresponds to events originating from reaction (2). The maximum of the second peak is at the pion mass squared $m^2_{\pi 0} = 18.2 \cdot 10^3$ MeV^2 as to be expected if events originated from reaction (1). The colored region represents the event distribution within the selection window for process (1).

The number of events simulated in the given bin i, $N_i^{(s)}$, is defined by the simulated luminosity $\mathcal{L}_s$ times the five-fold differential Born (non-radiative) cross section $d^5\sigma_s$ depending on variables Q^2, W, ϵ, $\cos\theta^*$ and ϕ convoluted with the radiative process and the experimental resolution. If we denote the contribution of the radiative processes (including internal and external bremsstrahlung) by $d\mathcal{R}_s$, and the simulated resolution response and acceptance of bin i by $\mathcal{K}_i^{(s)}$, the simulated number of events is then :

$$N_i^{(s)} = \mathcal{L}_s \int \left[d^5\sigma_{\rm model} \otimes d\mathcal{R}_s \otimes \mathcal{K}_i^{(s)} \right]. \qquad (12)$$

If the processes described by Eq. (12) are correctly taken into account in the simulation, then, assuming that the relative variation of the true cross section and the simulated one around a point $\mathcal{P}_0 = (W, Q^2, \epsilon, \cos\theta^*, \phi)$ are the same :

$$\frac{d\sigma(\mathcal{P}) - d\sigma(\mathcal{P}_0)}{d\sigma(\mathcal{P}_0)} = \frac{d\sigma_{\rm model}(\mathcal{P}) - d\sigma_{\rm model}(\mathcal{P}_0)}{d\sigma_{\rm model}(\mathcal{P}_0)} \ , \qquad (13)$$

we arrive at the experimental differential cross section at point $\mathcal{P}_0$:

$$d^5\sigma(\mathcal{P}_0) = \frac{\mathcal{L}_s}{\mathcal{L}} \times \frac{N_i}{N_i^{(s)}} \times d^5\sigma_{\rm model}(\mathcal{P}_0). \qquad (14)$$

These assumptions are verified *a posteriori* by observing a good agreement between the experimental and simulated distributions (e.g. missing mass spectra in Fig. 5). The size of the bins is only constrained by the magnitude of the resolution and radiative effects, and by the variation of the model cross section $d\sigma_{\rm model}$. In this analysis, we choose the point $\mathcal{P}_0$ to lie at the center of each bin.

2. *Adjustment of the model parameters*

The procedure described by Eq. 13 to evaluate the experimental cross section relies heavily on the accuracy of the simulation of the true cross section inside each bin by the model cross section $d\sigma_{\rm model}$. Thus, it is imperative to employ a realistic model cross section in the Monte Carlo simulation.

At the start of the analysis we used in the simulation and, consequently, in the determination of the experimental cross section, the MAID2000 model (see Section III A). It was found at this stage of the analysis that the model cross section departs from the measured one, especially for the second and third resonance regions. In particular we observed strong differences in the W, Q^2 and ϕ dependences of the cross sections which motivated an adjustment of the model parameters (see Section III B).

At the second step of the iteration the experimental cross sections were evaluated by employing the model version MAID2003 with the adjusted parameters. The adjustment did not involve model parameters responsible for the Q^2 dependence because the present data comprise a rather limited Q^2 interval. Instead we used our experimental results to obtain a better estimation of the Q^2 dependence. Another iteration was performed afterwards by including in the simulation the new Q^2 dependence (see Section IV). The final results are presented in Sections IV and V.

3. *Corrections and systematic errors*

In the extraction of the cross section values, a number of corrections have to be taken into account. For each correction, the residual systematic error was evaluated. All relevant quantities are given in Table III.

TABLE III: Correction and systematic error evaluation

Source	Correction	Induced error on σ
Trigger efficiency	1-10 %	±0.0 %
Acquisition dead time	0-30 %	±0.0 %
Electronics dead time	2.5-4.5 %	±0.1 %
VDCs efficiency	0.0 %	±0.0 %
Tracking efficiency	3.0-8.0 %	±0.5 %
Optics		±1.2 %
Acceptance		±2.0 %
Target boiling		±1.0 %
Target impurity	0.01 %	±0.0 %
Proton absorption correction	1-3 %	±0.1 %
Radiative corrections		±2.0 %
Photon contamination	1.0 %	±0.0 %
Quadratic sum		±3.3 %

The trigger efficiency correction $E_{1,2}(x, y)$ is calculated run by run for each scintillator plane (1 and 2), locally in longitudinal (x) and transverse (y) directions. The VDCs

determine the particle's track location in the scintillator. For this efficiency study, a stringent event selection in the four planes of the VDCs is applied. The efficiency correction factor is then (for the electron arm) :

$$E_{1,2}(x,y) \;=\; 1 + \frac{N(T_2.\overline{S_{1,2}}) \times PS_2}{N(T_5) + N(T_1) \times PS_1 + N(T_2.\overline{S_{1,2}}) \times PS_2} \;. \tag{15}$$

Here, $N(T_2.\overline{S_{1,2}})$ is the number of T2 trigger events tracked by the VDCs to the (x,y) area, but with no $S_1 \cap S_2$ scintillator coincidence. A similar procedure is applied for the hadron arm with the T4 triggers. The correction does not exceed 10 % for the electron arm, and is of the order of 1% for the hadron arm. The accuracy on this correction is governed by the number of T2 and T4 triggers, and is of the order of 1–5% of the inefficiency. This induces no appreciable systematic error in the final result.

The dead time correction factor of the acquisition system is the ratio of the number of events measured by the scaler associated to trigger T5 to the total number of coincidence events found in each run. It ranges from 0 to 30 % and the associated error is negligible.

The dead time associated with the electronics is defined by the setup and depends directly on the beam intensity. It is evaluated for each run from the singles rate of each discriminator associated with the scintillator paddles and electron Cherenkov. Typically, the correction is 2.5% at the $\Delta(1232)$ resonance, and 4.5% for the highest W setup. The induced systematic error is negligible.

The intrinsic efficiency of the VDCs is determined by the efficiency of each sense wire. A good track requires a signal from at least 3 wires in each plane. The fact that a typical track intercepts five cells in each wire plane makes the VDCs global inefficiency negligible.

The tracking efficiency is affected by accidental hits, caused by background events, which can prevent the algorithm from reconstructing the good track. Thus, a noticeable fraction of the events have more than one reconstructed track in the VDCs. These events are rejected in the analysis and the luminosity is decreased in proportion. Also this correction depends strongly on the setup configuration and on the beam current, and varies between 3% and 8%. The systematic error in this correction is estimated to be 10% of the correction.

Independent of the uncertainty in the total acceptance of the HRS pair, we have a cross section uncertainty from the imperfect knowledge of the spectrometer optics. We subdivide the acceptance into bins in the physics variables Q^2, W, M_X^2, $\cos\theta^*$, and ϕ. The precise volume of each bin is subject to uncertainties due to *local* variations in the average reconstruction of vertex variables. We estimate these uncertainties from the rms deviations between the positions of the sieve slit holes (at the entrance of each spectrometer) and the mean reconstructed position of these holes. Local variations in the calibration of vertex positions along the beam line influence the luminosity, which is proportional to the effective target length viewed by the HRS pair. We estimate the uncertainty in the effective target lengths from the deviations between the positions of a set of seven reference foil targets and their reconstructed positions. The sieve slit holes are on a square grid of spacing 25 mm vertical and 12.5 mm horizontal. The seven targets were located at 0, $\pm$20, $\pm$50, and $\pm$75 mm along the beam axis. In the electron arm, the rms deviations of the mean reconstructed values are 0.065 mm and 0.050 mm, for the vertical and horizontal sieve slit holes, respectively, and 0.145 mm for the target foils along the beam axis. The same values for the hadron arm are 0.097 mm, 0.027 mm, and 0.220 mm. Dividing the rms variations by the respective spacings in the vertical and horizontal sieve slit holes and the reference targets, we obtain the contributions to the cross section uncertainties arising from local variations in optics. Adding all contributions in quadrature yields an uncertainty of $\pm$1.2%. This is the optics uncertainty in Table III.

We have performed a set of acceptance cuts to improve the agreement between the experiment and the simulation (see Section II C 3). The uncertainty associated with possible residual discrepancies is estimated to be $\pm$2%.

The beam current and its variation can lead to target density corrections to the luminosity. The beam was rastered over an area proportional to the beam current, and equal to 8×8 mm^2 at 100 μA to minimize any effect of hydrogen boiling. ¿From analyses of single arm elastic data, we find the target density uncorrelated with beam current [37], within $\pm$1% drifts.

From the analysis of the single arm elastic data, it was also concluded that the target impurity is negligible, i.e. $\leq$ 0.02%.

A correction was also evaluated for lost recoil protons, either from interactions with the liquid hydrogen target material or in the different windows; its value equals 1% near the pion production threshold and reaches about 3% at the highest W.

The error associated with the radiative correction is $\pm$2%. This matter has been discussed in Section II C 2.

Finally, at low W, the contribution of reaction (2) is not negligible in the selected window in missing mass squared. A correction has been made to subtract the photon events located below the π^0 peak (see Fig. 5) ; it does not induce any further systematic error.

The total error evaluated as a quadratic sum of all the contributions amounts to $\pm$3.3 %. This total error will be added quadratically to the model dependence error discussed in Section V.

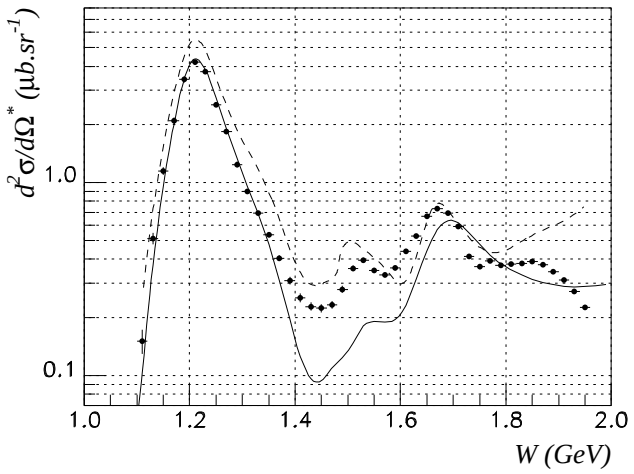

FIG. 6: Excitation curve for $\gamma^* p \to p\pi^0$ at $Q^2 = 1.0$ GeV^2, $\cos\theta^* = -0.975$, and $\phi = 75°$. The full line corresponds to MAID2000 [10] and the dashed line to SAID (NF18K solution) [11].

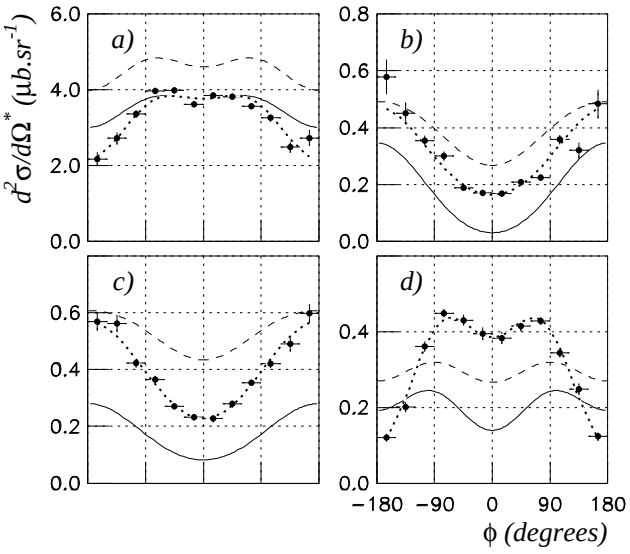

FIG. 7: Azimuthal angular distributions for $\gamma^* p \to p\pi^0$ at $Q^2 = 1.0$ GeV^2, $\cos\theta^* = -0.975$ for different points in W: 1230 MeV — a), 1410 MeV — b), 1550 MeV — c) and 1810 MeV — d). The solid curve corresponds to MAID2000 [10] and the dashed line to SAID (NF18K solution) [11]. The dotted line approximating the data points is the result of a second order polynomial fit in $\cos\phi$.

III. STUDY OF THE W, θ^* AND ϕ DEPENDENCES

A. Excitation curves and angular distributions

The method presented in Section II D is applied to produce the two-fold differential cross sections as a function of W, Q^2, $\cos\theta^*$ and ϕ. The cross section is evaluated in $50 \times 1 \times 4 \times 12$ kinematical intervals chosen as shown in Table IV. Fig. 6 shows a sample excitation curve for $Q^2 = 1.0$ GeV^2, $\cos\theta^* = -0.975$ and $\phi = 75°$.

TABLE IV: Binning intervals for each variable. Note that the analysis of the Q^2 dependence discussed in Section IV required splitting of the Q^2 range into 6 intervals as well as a wider binning in W and $\cos\theta^*$.

Variable	Range	Number of intervals	Interval width
W	[1.00;2.00] GeV	50(10)	0.02(0.1) GeV
Q^2	[0.85;1.15] GeV^2	1(6)	0.3(0.05) GeV^2
$\cos\theta^*$	[-1;-0.8]	4(1)	0.05(0.2)
ϕ	[0;360] °	12	30 °

The data integrated over the whole Q^2 range yield the cross section as a function of ϕ for each W and $\cos\theta^*$ interval. As an example, we present in Fig. 7 the azimuthal distributions for four points in W.

The corresponding cross sections evaluated in the framework of the MAID2000 model [10] demonstrate a good agreement with the results obtained in the $\Delta(1232)$ region. The agreement deteriorates as W increases (Figs. 6 and 7).

For each bin in W and $\cos\theta^*$, we obtain the separated cross sections $\sigma_{\rm T} + \epsilon\,\sigma_{\rm L}$, $\sigma_{\rm TL}$ and $\sigma_{\rm TT}$ by fitting a second order polynomial function in $\cos\phi$ on the data in 12 bins in ϕ (Fig. 7). In the procedure of minimization only the statistical errors are used.

The evident departure of the SAID analysis from the data observed even in the range of the $\Delta(1232)$ is explained by the lack of existing data for π^0 electroproduction in our kinematical range to constrain the NF18K solution. The agreement is restored after adding the results of the present experiment to the world database (see Section III C).

B. Amplitude Analysis with MAID

With our complete dataset of 363 data points in three observables and three values of pion emission angle we performed a data analysis using the unitary isobar model MAID2003. This model is based on the evaluation of a nonresonant background described by Born terms and vector meson exchange, and a resonant part modeled with Breit-Wigner functions for all four star nucleon resonances below $W = 2$ GeV,

$$t^{\alpha}_{\gamma\pi} = v^{bg,\alpha}_{\gamma\pi}(1 + i t^{\alpha}_{\pi}) + t^{BW,\alpha}_{\gamma\pi} e^{i\phi_\alpha}\,. \qquad (16)$$

Both parts are individually unitarized. For the background part this is done in the usual K-matrix approximation and for the resonance part by including an energy dependent unitarization phase ϕ_α. The background and the hadronic parameters of the resonances are fixed, leaving only the electromagnetic couplings of the N^*'s and

Δ's as free parameters. For electroproduction these are electric, magnetic and longitudinal couplings that can be expressed in terms of the helicity amplitudes $A_{1/2}$, $A_{3/2}$ and $S_{1/2}$. They are defined at the resonance position $W = M_R$ and are related to the transition form factors. In MAID2000 the Q^2 dependence of these couplings is modeled by semi-phenomenological form factors. In MAID2003 it has a phenomenological form fitted to all existing electroproduction data (global fit). Since our data are taken in a narrow interval around $Q^2 = 1.0$ GeV^2, the current analysis will be a fixed-Q^2 analysis (local fit).

From the 13 nucleon resonances below $W = 2$ GeV, 5 are fixed by the global fit and the remaining 8 resonances are fitted to the data. These are $P_{33}(1232)$, $P_{11}(1440)$, $D_{13}(1520)$, $S_{11}(1535)$, $S_{31}(1620)$, $S_{11}(1650)$, $F_{15}(1680)$ and $D_{33}(1700)$ giving a total of 20 free parameters. In order to get an estimate of the model uncertainty in our fit we have successively fixed individual resonance parameters to the values of the global fit and have investigated the fluctuations. In Table V we give the result of our fit for the 5 most stable resonances. The remaining S_{31}, S_{11} and D_{33} show big variations and are excluded in the table, even so, especially for the D_{33} a strong sensitivity can be seen in the energy region above $W = 1700$ MeV. The main reason for these fluctuations is the limited angular range of our dataset which is limited to backward angles only. Furthermore the lack of π^+ data makes the fit insensitive to the isospin of the resonances. The amplitudes are compared to the default values of MAID2000. For the $\Delta(1232)$ resonance we give in addition the $R_{EM} = E2/M1$ and the $R_{SM} = C2/M1$ ratios. Both are consistent with the previous MAID2000 fits to photo- and electroproduction data [10]. The R_{SM} ratio is very well determined by $\sigma_{\rm TL}$ and tends to larger negative values at $Q^2 = 1.0$ GeV^2 in comparison to $Q^2 = 0$, while the R_{EM} ratio is much more uncertain and also the model uncertainties are larger than for the $C2/M1$ ratio. From $\sigma_{\rm TL}$ we also find a large sensitivity to the S_{0+} amplitude of the $S_{11}(1535)$ resonance in the minimum around $W = 1500$ MeV.

TABLE V: Transverse and longitudinal helicity amplitudes $A_{1/2}$, $A_{3/2}$ and $S_{1/2}$ for electromagnetic excitation of nucleon resonances off the proton at $Q^2 = 1.0$ GeV^2 in units of $10^{-3}\,GeV^{-1/2}$. The default values of MAID2000 are compared to our local fit with the new version MAID2003. The $R_{EM} = E2/M1$ and $R_{SM} = C2/M1$ ratios of the $\Delta(1232)$ are given in percentage. The errors given for the amplitudes are first the statistical errors of the fit and second the estimated model uncertainty, the errors of the ratios include both and are mainly model uncertainties.

N^*		MAID2000 default values	MAID2003 local fit
$P_{33}(1232)$	$A_{1/2}$	-75	-70 ± 1 ± 2
	$A_{3/2}$	-142	-153 ± 3 ± 5
	$S_{1/2}$	15	18 ± 1 ± 2
	R_{EM}	-2.2	-5.6 ± 2.6
	R_{SM}	-6.5	-7.7 ± 1.7
$P_{11}(1440)$	$A_{1/2}$	-61	7 ± 5 ± 20
	$S_{1/2}$	20	34 ± 3 ± 10
$D_{13}(1520)$	$A_{1/2}$	-69	-86 ± 4 ± 20
	$A_{3/2}$	38	44 ± 9 ± 10
	$S_{1/2}$	0	2 ± 4 ± 10
$S_{11}(1535)$	$A_{1/2}$	67	41 ± 5 ± 25
	$S_{1/2}$	0	-17 ± 3 ± 10
$F_{15}(1680)$	$A_{1/2}$	-42	-31 ± 3 ± 10
	$A_{3/2}$	51	27 ± 7 ± 10
	$S_{1/2}$	0	-30 ± 2 ± 10

C. New Solution from SAID Analysis

There exists also another well developed technique for describing pion electroproduction data for the whole resonance region — the SAID analysis [11, 12]. It employs the most complete compilation of the data available in several photo- and electroproduction reactions which makes it possible to constrain 173 parameters used in the evaluation of the cross sections.

The prediction of the SAID analysis corresponding to the parameter set NF18K [11] is shown in Figs. 6,7. The analysis is not expected to yield meaningful results in the event of extrapolation into the new kinematic domain which is investigated in the present experiment. This explains the departure of the dashed curve from the data observed in Figs. 6,7. The new solution obtained by I. Strakovsky by complementing the world database with our data set is labelled as GF20 [12] and is shown in Fig. 10 (see Section V). We find a noticeable agreement between our results and the solution GF20 of the SAID analysis in the region of $P_{33}(1232)$ for the differential cross sections. As in the case of the MAID2000 model, the agreement declines in the second and the third resonance regions.

We can therefore summarise that within the kinematical region under study the discrepancies between the results of the MAID2000 model and SAID analysis increase with the increase in W, that is, in the region where data on π^0 electroproduction are scarce.

D. θ^* dependence

Kinematical restrictions of the present experiment allow us to reliably reconstruct the event distributions as a function of the pion angle θ^* only in a rather narrow interval $-1 \leq cos\theta^* \leq -0.8$. The corresponding cross section is shown in Fig. 8 after completing optimization of the MAID2000 parameters.

Overall, the relative shape in θ^* of the MAID2003 model compared to the experimental data is good for all bins in W. One should notice that the normalization discrepancy observed in Fig. 8i is due to the W dependence of the cross section and not to the θ^* dependence.

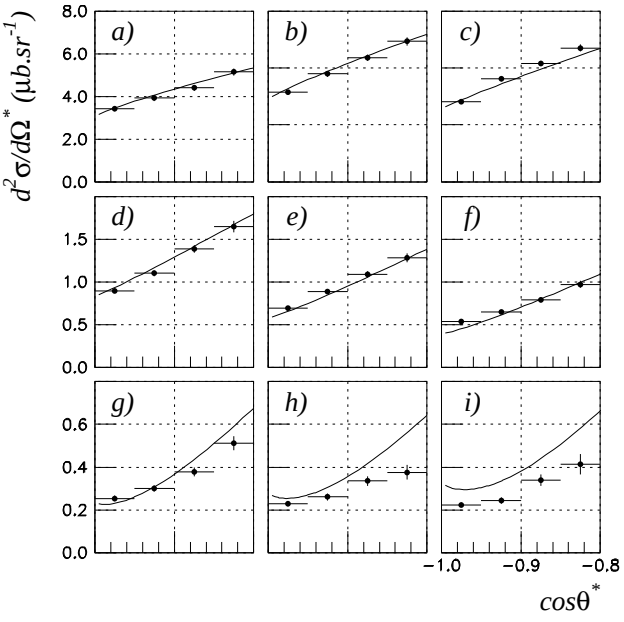

FIG. 8: Cross sections of reaction (1) as a function of $cos\theta^*$ obtained at $Q^2 = 1.0$ GeV^2, $\phi = 75^\circ$ for different points in W: 1190 MeV — a), 1210 MeV — b), 1230 MeV — c), 1310 MeV — d), 1330 MeV — e), 1350 MeV — f), 1410 MeV — g), 1430 MeV — h) and 1450 MeV — i). In all plots, $-1.0 \leq \cos\theta^* \leq -0.8$. The solid curve corresponds to MAID2003.

IV. STUDY OF THE Q^2 DEPENDENCE

We considered the existing correlation between ϕ and Q^2 due to the acceptance as a possible source of systematic errors. To minimize this effect, we need a more realistic Q^2 dependence in the model. To this end we first extract the experimental Q^2 dependence for each bin in W and, second, iterate the analysis using a model cross section $d\sigma_{\rm model}$ that includes the determined dependence.

The cross sections were evaluated by splitting our Q^2 range [0.85, 1.15] GeV^2 into six intervals, integrating over cosθ^* in the range [–1.0,–0.8], and fitting the ϕ dependence of the cross section in a similar way to that described in Section III.

The Q^2 dependence of the cross section can be studied by fitting the following form on the partial $\sigma_{\rm T}+\epsilon\,\sigma_{\rm L}$ cross section :

$$d\sigma(W,Q^2) = d\sigma(W,Q^2=1\,{\rm GeV}^2)\cdot e^{-b_{\rm exp}\cdot(1\,{\rm GeV}^2-Q^2)} \quad (17)$$

The resulting fit values for $b_{\rm exp}$ are displayed in Fig. 9. We perform a similar exercise with the cross section evaluated within the MAID2000 model and the GF20 SAID model. The resulting parameters $b_{\rm maid}(W)$ and $b_{\rm said}(W)$ are displayed in Fig. 9 respectively with a full and a dashed curves. While the overall ranges of variation of $b_{\rm exp}$, $b_{\rm maid}$ and $b_{\rm said}$ are consistent, we observe a substantial discrepancy between the models and the data in the range of W from ~ 1.25 to ~ 1.65 GeV.

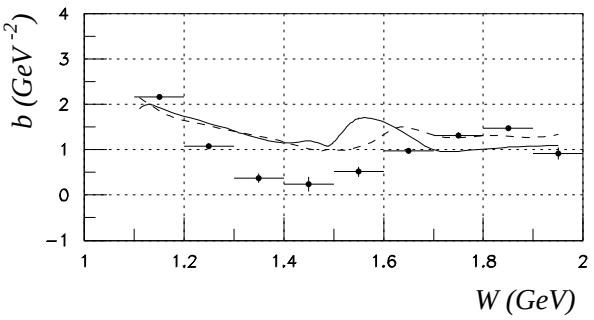

FIG. 9: Q^2 evolution of $\sigma_{\rm T} + \epsilon\,\sigma_{\rm L}$ evaluated at a central Q^2 = 1.0 GeV^2 from the data points. The solid curve corresponds to MAID2000 and the dashed line to SAID (parameters GF20) [12]. See text for definition of b.

The data obtained in the present analysis allow us to determine the Q^2 dependence of the partial cross section $\sigma_{\rm T} + \epsilon\,\sigma_{\rm L}$ in a wide range of W which at this time was not possible in other experiments on exclusive pion electroproduction. In principle, it is also feasible to study the Q^2 dependence of the partial cross sections $\sigma_{\rm TT}$ and $\sigma_{\rm TL}$. However, such an analysis would require much more statistics in order to allow a meaningful interpretation.

The experimental Q^2 dependence of Eq. 17 is used in our final data analysis with MAID2003 parameters. In addition, we compute a systematic error associated with the Q^2-dependent interpolation in the data analysis. This systematic error is evaluated from one half of the difference between the final analysis and the results obtained from the analysis using the MAID2003 model without additional Q^2-dependence.

V. DISCUSSION AND CONCLUSIONS

The final cross sections we obtained are listed in Tables VI, VII and VIII [38]. The value of ϵ indicated in these tables corresponds to a fixed value of $k = 4032$ MeV within each considered interval in W.

Fig. 10 presents the cross sections $\sigma_{\rm T} + \epsilon\,\sigma_{\rm L}$, $\sigma_{\rm TL}$ and $\sigma_{\rm TT}$ as a function of W, evaluated at $\cos\theta^* = -0.975$.

The systematic errors obtained according to the iterative procedure described in Section IV are added quadratically to the errors of Table III. The total systematic error is represented in Tables VI,VII, VIII and in Fig. 10. It is of the same order as the statistical error. Even though the relative precision in determining $\sigma_{\rm TL}$ and $\sigma_{\rm TT}$ is worse than that of $\sigma_{\rm T} + \epsilon\,\sigma_{\rm L}$, it is still large enough to observe unambiguously the sign and sign changes of the interference terms $\sigma_{\rm TL}$ and $\sigma_{\rm TT}$.

The parameter $b_{\rm exp}$ introduced in Section IV can be phenomenologically related with the scale parameter Λ, which determines the Q^2 dependence of hadronic form factors and resonance multipoles via the dipole approxi-

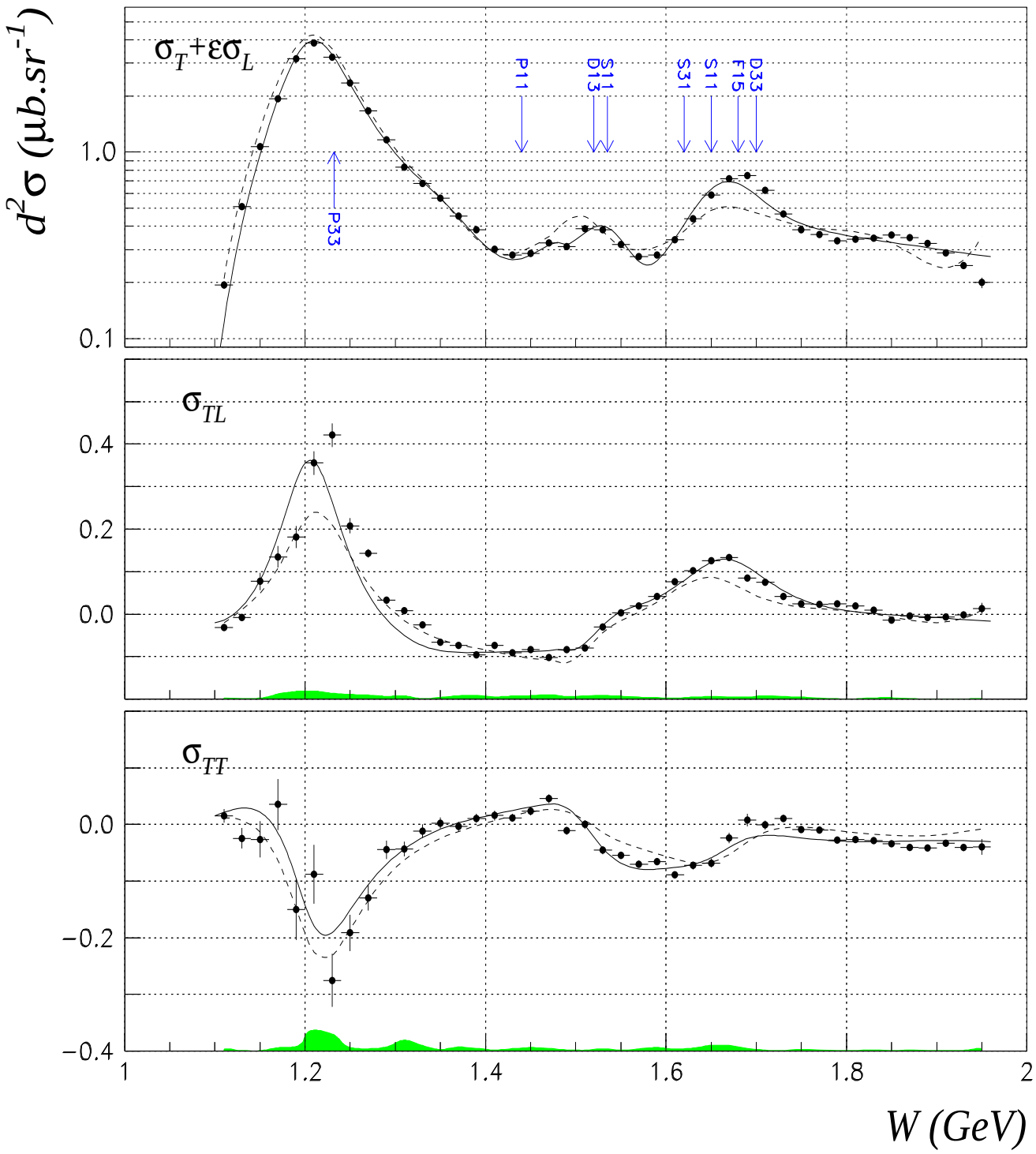

FIG. 10: Virtual photo-production cross sections for $\gamma^* p \to p\pi^0$ with statistical error bars as a function of W at $Q^2 = 1.0$ GeV^2, $\cos\theta^* = -0.975$: $\sigma_{\rm T} + \epsilon\ \sigma_{\rm L}$, $\sigma_{\rm TL}$ and $\sigma_{\rm TT}$. The one-sigma value of the total systematic errors is given for the $\sigma_{\rm TL}$ and $\sigma_{\rm TT}$ cross sections by the size of the shaded area at the bottom of each plot. Solid curves correspond to MAID2003 with the set of parameters extracted from our results, and dashed curves correspond to the SAID GF20 solution [12]. In the top part of the figure, we indicated the positions of the 8 most prominent resonances whose helicity amplitudes are adjusted in MAID2000 (see Section III B).

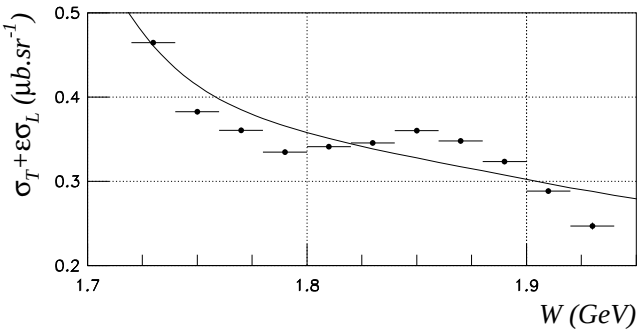

FIG. 11: Zoom of the $\sigma_{\rm T}+\epsilon\ \sigma_{\rm L}$ cross section around the high W region at $Q^2 = 1.0$ GeV^2, $\cos\theta^* = --0.975$. The full line corresponds to MAID2003.

mation:

$$G_{\rm D}(Q^2) = \frac{1}{(1+Q^2/\Lambda^2)^2}\ , \qquad (18)$$

Assuming that $d^2\sigma(Q^2) \sim (G_{\rm D}(Q^2))^2$ one finds that $b_{\rm exp} \approx 4/(Q^2+\Lambda^2)$. Therefore $b_{\rm exp} \to 0$ when the target is structureless ($\Lambda^2 \to \infty$), $b_{\rm exp} \to 4/Q^2 = 4$ GeV^{-2} at $Q^2 = 1$ GeV^2 in the case $\Lambda^2 \ll Q^2$. For the standard dipole $\Lambda^2 = 0.71$ GeV^2, and at $Q^2 = 1$ GeV^2 one has $b_{\rm exp} = 2.3$ GeV^{-2}.

The range of observed variations of the parameter b_{exp} displayed in Fig. 9 lies essentially within the limits $0 < b_{\rm exp} < 4$ GeV^2. Thus, it is consistent with the simplest approximation suggested by the Q^2 dependence of the dipole form factor discussed above.

While Eq. (18) provides a reasonable approximation for nucleon form factors in the range of Q^2 considered in this study, it is known to deviate [39] from the results obtained for the γNΔ transition form factor $G_M^*(Q^2)$ which describes the dominant magnetic dipole excitation of the $\Delta(1232)$. In particular, $G_M^*(Q^2)$ falls off faster with Q^2 than the dipole form factor indicating a larger magnetic radius for the resonance state than that of the nucleon [22]. Our results on $b_{\rm exp}$ yield new information on this topic especially for $W > 1.7$ GeV even if the separation of contributions from resonant and nonresonant amplitudes has not been achieved.

Nontrivial W dependence of the parameter $b_{\rm exp}$ results from interplay between contributions of the resonant and nonresonant amplitudes. The latter are known to be small around the $\Delta(1232)$ and increase monotonically with W. We find from the data that $b_{\rm exp} \approx 0$ in the range of $1.3 < W < 1.4$ GeV, which indicates cancellation of the different Q^2 dependences of the resonant (especially P_{11}–Roper) and nonresonant amplitudes. The dominance of the resonant amplitude M_{1+} in the range $W < 1.3$ GeV results in $b_{\rm exp} \approx 1-2$ GeV^{-2}, and $b_{\rm exp} \approx 1-1.5$ GeV^{-2} in the range $W > 1.6$ GeV where nonresonant terms start to dominate.

In summary, we have measured in the resonance region the three partial cross sections $\sigma_{\rm T} + \epsilon\ \sigma_{\rm L}$, $\sigma_{\rm TT}$, and $\sigma_{\rm TL}$ for the reaction $\gamma^* p \to p\pi^0$ at Q^2=1 GeV^2 and backward angle. We have obtained the Q^2 dependence for the cross section integrated over the variable ϕ : $\int d\sigma\ d\phi = \sigma_{\rm T} + \epsilon\ \sigma_{\rm L}$. These data will be used to constrain models. A first step was done for the Unitary Isobar Model MAID2000 [10]. In spite of the agreement between our data and the calculation, the Q^2 dependence of the total cross section is not reproduced by the model.

The MAID2000 and SAID analyses employ fundamentally different techniques for finding model parameters. By examining deviations of the results of the available models for resonance excitations from the measurements presented in this article we find appreciable discrepancies in a major part of the kinematics under study (backward pion electroproduction). We note a poor agreement in the high W region both between the models and between each model and the data. The results of model calculations both from MAID2000 and SAID demonstrated initially very poor agreement with our data, but a joint analysis with the world dataset resulted in a much improved description of the data. This is explained by evident limitations in the kinematics of the pre-existing dataset for even the relatively simple $\gamma^* p \to p\pi^0$ reaction, particularly at high W. From the MAID2000 analysis, we find new constraints on the R_{EM} and R_{SM} ratios of the $\Delta(1232)$ resonance (Table V).

Finally, although our results are not sufficient to allow a full partial-wave analysis in the high W region (between 1.7 and 2.0 GeV), the position of the enhancement of $\sigma_{\rm T} + \epsilon\ \sigma_{\rm L}$ (see Fig. 11) is fully consistent with the recent analysis of Chen *et al.* [40]. The dynamical model used in [40] implies that the third S_{11} resonance should have the mass 1846 ± 47 MeV. Evidences of missing resonances in this region have also been shown in pion electroproduction at CLAS [41], in kaon photoproduction at SAPHIR [42] and CLAS [44], and in $\pi N \to \pi\eta$ [43]. All these recent publications demonstrate the interest of both theoreticians and experimentalists in a detailed understanding of the nucleon resonance region, and point out the need for accurate data in meson electro- and photoproduction.

The underlying physics of the nucleon resonances and the transition to deep inelastic scattering is still under investigation. Therefore, new data on exclusive processes as a function of both W and Q^2 are of great value.

Acknowledgments

We wish to acknowledge the staff of the accelerator who delivered the beam, as well as the Hall A technical staff. This work was supported by DOE contract DE-AC05-84ER40150 under which the Southeastern Universities Research Association (SURA) operates the Thomas Jefferson National Accelerator Facility. We acknowledge additional grants from the US DOE and NSF, the French Centre National de la Recherche Scientifique and Commissariat à l'Energie Atomique, the Conseil Régional d'Auvergne, the FWO-Flanders (Belgium) and the BOF-Gent University. We also wish to thank Igor Strakovsky for his participation in the discussion of the theoretical part and model calculations.

[1] P.Y. Bertin, C. Hyde-Wright, P.A.M. Guichon *et al.*, "Nucleon Structure Study by Virtual Compton Scattering," CEBAF proposal PR93050 (1993) ; http://www.jlab.org/exp_prog/proposals/93/PR93-050.pdf .
[2] N. Isgur and G. Karl, Phys. Rev. D **19**, 2653 (1979) [Erratum-ibid. D **23**, 817 (1981)].
[3] R. Koniuk and N. Isgur, Phys. Rev. Lett. **44**, 845 (1980).
[4] R. Koniuk and N. Isgur, Phys. Rev. D **21**, 1868 (1980) [Erratum-ibid. D **23**, 818 (1980)].
[5] R. Koniuk, Nucl. Phys. B **195**, 452 (1982).
[6] S. Capstick and W. Roberts, Phys. Rev. D **49**, 4570 (1994) [arXiv:nucl-th/9310030].
[7] R. Bijker, F. Iachello and A. Leviatan, Phys. Rev. C **54**, 1935 (1996) [arXiv:nucl-th/9510001].
[8] I. Niculescu *et al.*, Phys. Rev. Lett. **85**, 1186 (2000).
[9] I. Niculescu *et al.*, Phys. Rev. Lett. **85**, 1182 (2000).
[10] D. Drechsel, O. Hanstein, S. S. Kamalov and L. Tiator, Nucl. Phys. A **645**, 145 (1999); http://www.kph.uni-mainz.de/MAID/. S. S. Kamalov, D. Drechsel, O. Hanstein, L. Tiator and S. N. Yang, Nucl. Phys. A **684**, 321 (2001).
[11] R. A. Arndt, I. I. Strakovsky and R. L. Workman, Phys. Rev. C **53**, 430 (1996) [arXiv:nucl-th/9509005] ; http://gwdac.phys.gwu.edu .
[12] R. A. Arndt, I. I. Strakovsky, and R. L. Workman, "Analysis of pion electroproduction data," in: *Proc. of 9th International Symposium on Meson-Nucleon Physics and the Structure of the Nucleon, Washington, DC, USA, July 26–31, 2001*, Eds. H. Haberzettl and W. J. Briscoe, πN Newslett. **16**, 150–153 (2002); Eprint nucl-th/0110001.
[13] R. M. Davidson, N. C. Mukhopadhyay and R. S. Wittman, Phys. Rev. D **43**, 71 (1991).
[14] I. G. Aznaurian, Phys. Rev. D **57**, 2727 (1998) [arXiv:hep-ph/9708238].
[15] I. G. Aznauryan, Phys. Rev. C **67**, 015209 (2003) [arXiv:nucl-th/0206033].
[16] NSTAR 2001, Proceedings of the Workshop on the Physics of Excited Nucleons, Germany, edited by D. Drechsel and L. Tiator, published in World Scientific 2001 .
[17] R. Siddle *et al.*, Nucl. Phys. B **35**, 93 (1971).
[18] S. Galster *et al.*, Phys. Rev. D **5**, 519 (1972).
[19] J. C. Alder *et al.*, Nucl. Phys. B **46**, 573 (1972).
[20] W. Albrecht *et al.*, Nucl. Phys. B **25**, 1 (1970).
[21] W. Albrecht *et al.*, Nucl. Phys. B **27**, 615 (1971).
[22] V. V. Frolov *et al.*, Phys. Rev. Lett. **82**, 45 (1999) [arXiv:hep-ex/9808024].
[23] K. Joo *et al.* [CLAS Collaboration], Phys. Rev. Lett. **88**, 122001 (2002) [arXiv:hep-ex/0110007].
[24] Basic Instrumentation for Hall A at Jefferson Lab, to be published in Nuclear Instruments and Methods.
[25] J. Denard, A. Saha and G. Lavessiere, PAC-2001-WPAH103 *Presented at IEEE Particle Accelerator Conference (PAC2001), Chicago, Illinois, 18-22 Jun 2001*
[26] K. B. Unser, CERN-SL-91-42-BI (1991), & AIP Conf. Proc. **252**, 266 (1991).
[27] Beam Postion Studies for E93050, C. Hyde-Wright, L. Todor G. Laveissière, JLab-TN-01-001.
[28] Hall A cryogenic and dummy targets information, R. Suleiman, JLab-TN-98-007.
[29] Vertical Drift Chambers for the Hall A High Resolution Spectrometers at Jefferson Lab, K.G. Fissum et al., JLab-TN-00-016.
[30] Cebaf Online Data Acquisition: http://coda.jlab.org .
[31] E.A.J.M. Offermann *et al.*, ESPACE Users's Guide, unpublished (1997); http://hallaweb.jlab.org/espace/docs.html .
[32] S. Jaminion, Thèse de doctorat, Université Blaise Pascal, DU 1259 (2001).
[33] L. Van Hoorebeke, in preparation.
[34] M. Vanderhaeghen, J. M. Friedrich, D. Lhuillier, D. Marchand, L. Van Hoorebeke and J. Van de Wiele, Phys. Rev. C **62**, 025501 (2000) [arXiv:hep-ph/0001100].
[35] A. Afanasev, I. Akushevich, V. Burkert and K. Joo, Phys. Rev. D **66**, 074004 (2002) [arXiv:hep-ph/0208183].
[36] G. Laveissière, Thèse de doctorat, Université Blaise Pascal, DU 1309 (2001).
[37] C. Jutier, PhD Thesis, Old Dominion University and Université Blaise Pascal, DU 1298 (2001).
[38] tables available at http://hallaweb.jlab.org/experiment/E93-050/vcs.l
[39] G. Sterman and P. Stoler, Ann. Rev. Nucl. Part. Sci., 47 (1997) 193. [arXiv:hep-ph/9708370].
[40] G. Y. Chen, S. Kamalov, S. N. Yang, D. Drechsel and L. Tiator, arXiv:nucl-th/0210013.
[41] M. Ripani, V. D. Burkert, V. Mokeev, M. Battaglieri, R. De Vita, E. Golovach and M. Taiuti, arXiv:hep-ex/0304034.
[42] T. Mart and C. Bennhold, Phys. Rev. C **61**, 012201 (2000) [arXiv:nucl-th/9906096].
[43] S. Capstick, T. S. Lee, W. Roberts and A. Svarc, Phys. Rev. C **59**, 3002 (1999) [arXiv:nucl-th/9904005].
[44] J.W.C. McNabb *et al.* in preparation.

TABLE VI: $\sigma_T + \epsilon\,\sigma_L$ cross section at $Q^2 = 1.0$ GeV^2 in $\mu b.sr^{-1}$. The values are followed by the statistical and the total systematic errors.

W (MeV)	ϵ	$\cos\theta^* = -0.975$			$\cos\theta^* = -0.925$			$\cos\theta^* = -0.875$			$\cos\theta^* = -0.825$		
1110.0	0.945	0.194	±0.009	±0.007	0.241	±0.013	±0.008	0.300	±0.020	±0.010	0.333	±0.033	±0.011
1130.0	0.944	0.511	±0.012	±0.017	0.597	±0.026	±0.020	0.721	±0.050	±0.025	0.756	±0.065	±0.026
1150.0	0.942	1.068	±0.024	±0.036	1.041	±0.066	±0.035	1.111	±0.090	±0.039	1.251	±0.104	±0.045
1170.0	0.940	1.937	±0.033	±0.067	2.365	±0.066	±0.082	1.676	±0.122	±0.057	2.795	±0.289	±0.109
1190.0	0.938	3.176	±0.035	±0.111	3.591	±0.072	±0.128	4.270	±0.168	±0.160	4.900	±0.361	±0.175
1210.0	0.936	3.853	±0.035	±0.137	4.264	±0.107	±0.158	4.790	±0.183	±0.208	3.585	±0.249	±0.189
1230.0	0.934	3.221	±0.034	±0.112	3.781	±0.128	±0.129	4.120	±0.180	±0.155	4.913	±0.269	±0.213
1250.0	0.932	2.348	±0.023	±0.082	2.645	±0.045	±0.091	2.548	±0.163	±0.090	2.966	±0.293	±0.128
1270.0	0.930	1.665	±0.015	±0.058	1.832	±0.028	±0.063	1.943	±0.089	±0.066	2.020	±0.340	±0.161
1290.0	0.927	1.162	±0.010	±0.040	1.317	±0.027	±0.047	1.366	±0.068	±0.048	1.307	±0.130	±0.052
1310.0	0.925	0.832	±0.009	±0.030	0.911	±0.030	±0.039	0.999	±0.061	±0.052	1.203	±0.112	±0.078
1330.0	0.922	0.680	±0.009	±0.024	0.686	±0.028	±0.023	0.861	±0.056	±0.039	0.850	±0.104	±0.031
1350.0	0.920	0.566	±0.009	±0.020	0.641	±0.024	±0.022	0.758	±0.061	±0.028	1.057	±0.137	±0.036
1370.0	0.917	0.455	±0.007	±0.016	0.513	±0.024	±0.019	0.484	±0.061	±0.034	0.235	±0.126	±0.008
1390.0	0.914	0.385	±0.007	±0.014	0.386	±0.025	±0.023	0.509	±0.067	±0.052	0.530	±0.178	±0.063
1410.0	0.910	0.301	±0.007	±0.011	0.370	±0.026	±0.023	0.409	±0.061	±0.040	0.141	±0.109	±0.039
1430.0	0.907	0.281	±0.006	±0.012	0.344	±0.022	±0.016	0.634	±0.082	±0.034	0.658	±0.165	±0.049
1450.0	0.903	0.286	±0.005	±0.011	0.380	±0.020	±0.020	0.390	±0.069	±0.025	0.545	±0.241	±0.029
1470.0	0.900	0.327	±0.006	±0.013	0.342	±0.026	±0.020	0.580	±0.114	±0.038			
1490.0	0.896	0.311	±0.005	±0.011	0.492	±0.035	±0.032	0.666	±0.105	±0.062			
1510.0	0.892	0.388	±0.005	±0.014	0.442	±0.026	±0.016	0.532	±0.097	±0.022			
1530.0	0.887	0.383	±0.005	±0.013	0.497	±0.023	±0.017	0.808	±0.125	±0.028			
1550.0	0.883	0.319	±0.004	±0.011	0.412	±0.037	±0.023	0.071	±0.177	±0.007			
1570.0	0.878	0.276	±0.004	±0.009	0.517	±0.043	±0.035	0.374	±0.365	±0.022			
1590.0	0.873	0.281	±0.004	±0.011	0.410	±0.040	±0.014	0.010	±0.140	±0.048			
1610.0	0.868	0.339	±0.004	±0.014	0.437	±0.028	±0.019	−0.032	±0.162	±0.004			
1630.0	0.863	0.439	±0.004	±0.018	0.491	±0.047	±0.023						
1650.0	0.857	0.590	±0.004	±0.028	0.687	±0.064	±0.046						
1670.0	0.852	0.719	±0.005	±0.041	0.721	±0.066	±0.057						
1690.0	0.845	0.749	±0.007	±0.048	0.738	±0.085	±0.026						
1710.0	0.839	0.625	±0.005	±0.035	0.519	±0.016	±0.019						
1730.0	0.832	0.465	±0.003	±0.024	0.397	±0.046	±0.025						
1750.0	0.826	0.383	±0.003	±0.017	0.300	±0.030	±0.016						
1770.0	0.818	0.361	±0.003	±0.013	0.153	±0.060	±0.007						
1790.0	0.811	0.335	±0.003	±0.011									
1810.0	0.803	0.341	±0.003	±0.012									
1830.0	0.795	0.346	±0.003	±0.012									
1850.0	0.786	0.360	±0.003	±0.012									
1870.0	0.777	0.348	±0.003	±0.012									
1890.0	0.768	0.323	±0.003	±0.011									
1910.0	0.759	0.288	±0.003	±0.010									
1930.0	0.749	0.247	±0.004	±0.009									
1950.0	0.738	0.200	±0.013	±0.007									

TABLE VII: $\sigma_{\rm TL}$ cross section at $Q^2 = 1.0$ GeV^2 in $\mu b.sr^{-1}$. The values are followed by the statistical and the total systematic errors.

W (MeV)	ϵ	$\cos\theta^* = -0.975$			$\cos\theta^* = -0.925$			$\cos\theta^* = -0.875$			$\cos\theta^* = -0.825$		
1110.0	0.945	−0.032	±0.007	±0.001	−0.087	±0.011	±0.003	−0.076	±0.017	±0.003	−0.096	±0.028	±0.003
1130.0	0.944	−0.008	±0.009	±0.001	−0.039	±0.023	±0.002	−0.093	±0.043	±0.004	−0.096	±0.055	±0.005
1150.0	0.942	0.077	±0.020	±0.003	0.150	±0.057	±0.005	0.261	±0.077	±0.011	0.184	±0.087	±0.011
1170.0	0.940	0.135	±0.025	±0.012	0.094	±0.054	±0.020	0.853	±0.101	±0.031	0.164	±0.236	±0.028
1190.0	0.938	0.182	±0.026	±0.018	0.418	±0.061	±0.033	0.240	±0.140	±0.054	0.043	±0.294	±0.054
1210.0	0.936	0.356	±0.028	±0.019	0.577	±0.095	±0.053	0.784	±0.157	±0.089	2.066	±0.206	±0.102
1230.0	0.934	0.421	±0.028	±0.014	0.611	±0.111	±0.029	0.911	±0.152	±0.061	0.797	±0.219	±0.104
1250.0	0.932	0.208	±0.018	±0.011	0.502	±0.037	±0.025	0.965	±0.135	±0.049	1.070	±0.239	±0.088
1270.0	0.930	0.143	±0.010	±0.010	0.293	±0.023	±0.017	0.504	±0.074	±0.026	0.775	±0.275	±0.143
1290.0	0.927	0.032	±0.008	±0.007	0.186	±0.024	±0.015	0.375	±0.057	±0.024	0.647	±0.107	±0.046
1310.0	0.925	0.008	±0.007	±0.008	0.113	±0.027	±0.032	0.292	±0.047	±0.047	0.298	±0.083	±0.071
1330.0	0.922	−0.025	±0.008	±0.001	0.067	±0.025	±0.009	0.073	±0.045	±0.038	0.273	±0.074	±0.037
1350.0	0.920	−0.066	±0.007	±0.004	−0.056	±0.020	±0.009	−0.050	±0.050	±0.026	−0.170	±0.103	±0.026
1370.0	0.917	−0.073	±0.006	±0.008	−0.076	±0.020	±0.012	0.036	±0.051	±0.035	0.317	±0.099	±0.021
1390.0	0.914	−0.096	±0.006	±0.008	−0.047	±0.020	±0.019	−0.084	±0.048	±0.039	−0.025	±0.120	±0.046
1410.0	0.910	−0.073	±0.006	±0.005	−0.105	±0.021	±0.023	−0.076	±0.045	±0.037	0.156	±0.078	±0.037
1430.0	0.907	−0.091	±0.005	±0.007	−0.110	±0.018	±0.017	−0.284	±0.062	±0.034	−0.240	±0.123	±0.048
1450.0	0.903	−0.084	±0.004	±0.008	−0.162	±0.017	±0.021	−0.099	±0.055	±0.029	−0.165	±0.182	±0.036
1470.0	0.900	−0.102	±0.005	±0.011	−0.109	±0.018	±0.017	−0.158	±0.056	±0.036			
1490.0	0.896	−0.083	±0.005	±0.007	−0.161	±0.025	±0.032	−0.174	±0.061	±0.057			
1510.0	0.892	−0.079	±0.005	±0.008	−0.065	±0.021	±0.019	−0.047	±0.065	±0.029			
1530.0	0.887	−0.030	±0.004	±0.009	−0.023	±0.018	±0.021	−0.132	±0.082	±0.038			
1550.0	0.883	0.004	±0.003	±0.007	0.022	±0.021	±0.030	0.264	±0.077	±0.031			
1570.0	0.878	0.019	±0.003	±0.005	0.020	±0.026	±0.039	0.258	±0.077	±0.039			
1590.0	0.873	0.041	±0.003	±0.003	0.076	±0.027	±0.022	0.109	±0.099	±0.043			
1610.0	0.868	0.076	±0.003	±0.003	0.121	±0.020	±0.006	0.384	±0.098	±0.017			
1630.0	0.863	0.102	±0.003	±0.005	0.164	±0.025	±0.008						
1650.0	0.857	0.125	±0.004	±0.006	0.193	±0.034	±0.026						
1670.0	0.852	0.133	±0.005	±0.005	0.292	±0.038	±0.031						
1690.0	0.845	0.085	±0.006	±0.005	0.146	±0.038	±0.005						
1710.0	0.839	0.075	±0.005	±0.008	0.122	±0.040	±0.005						
1730.0	0.832	0.041	±0.003	±0.006	0.133	±0.027	±0.018						
1750.0	0.826	0.025	±0.003	±0.005	0.031	±0.018	±0.011						
1770.0	0.818	0.023	±0.003	±0.003	0.031	±0.036	±0.015						
1790.0	0.811	0.024	±0.002	±0.001									
1810.0	0.803	0.020	±0.003	±0.001									
1830.0	0.795	0.010	±0.003	±0.003									
1850.0	0.786	−0.014	±0.002	±0.003									
1870.0	0.777	−0.004	±0.002	±0.001									
1890.0	0.768	−0.008	±0.003	±0.000									
1910.0	0.759	−0.006	±0.003	±0.000									
1930.0	0.749	−0.002	±0.004	±0.000									
1950.0	0.738	0.014	±0.013	±0.000									

TABLE VIII: $\sigma_{\rm TT}$ cross section at $Q^2 = 1.0$ GeV^2 in $\mu b.sr^{-1}$. The values are followed by the statistical and the total systematic errors.

W (MeV)	ϵ	$\cos\theta^* = -0.975$			$\cos\theta^* = -0.925$			$\cos\theta^* = -0.875$			$\cos\theta^* = -0.825$		
1110.0	0.945	0.015	±0.012	±0.001	0.038	±0.015	±0.002	0.044	±0.024	±0.002	0.022	±0.034	±0.001
1130.0	0.944	−0.024	±0.018	±0.001	−0.016	±0.031	±0.001	−0.019	±0.050	±0.001	0.069	±0.061	±0.004
1150.0	0.942	−0.026	±0.032	±0.001	−0.197	±0.066	±0.007	−0.293	±0.082	±0.011	−0.225	±0.092	±0.013
1170.0	0.940	0.036	±0.045	±0.006	0.040	±0.066	±0.014	−0.803	±0.105	±0.027	−0.498	±0.208	±0.037
1190.0	0.938	−0.150	±0.054	±0.008	−0.358	±0.090	±0.015	−0.254	±0.157	±0.029	−0.507	±0.279	±0.021
1210.0	0.936	−0.088	±0.052	±0.037	−0.414	±0.124	±0.017	−0.732	±0.187	±0.046	−2.378	±0.253	±0.092
1230.0	0.934	−0.275	±0.047	±0.030	−0.584	±0.128	±0.067	−0.986	±0.165	±0.047	−0.888	±0.242	±0.035
1250.0	0.932	−0.191	±0.032	±0.007	−0.558	±0.051	±0.040	−0.918	±0.133	±0.050	−1.137	±0.226	±0.040
1270.0	0.930	−0.129	±0.023	±0.004	−0.391	±0.038	±0.022	−0.571	±0.080	±0.036	−1.000	±0.242	±0.072
1290.0	0.927	−0.045	±0.016	±0.007	−0.236	±0.037	±0.009	−0.584	±0.071	±0.023	−0.818	±0.120	±0.028
1310.0	0.925	−0.043	±0.013	±0.019	−0.153	±0.036	±0.007	−0.290	±0.073	±0.015	−0.357	±0.125	±0.036
1330.0	0.922	−0.012	±0.012	±0.010	−0.168	±0.029	±0.024	−0.180	±0.057	±0.006	−0.331	±0.116	±0.027
1350.0	0.920	0.002	±0.010	±0.003	−0.034	±0.022	±0.015	−0.013	±0.053	±0.009	0.064	±0.123	±0.043
1370.0	0.917	−0.004	±0.009	±0.007	0.007	±0.023	±0.001	−0.177	±0.052	±0.012	−0.444	±0.108	±0.024
1390.0	0.914	0.011	±0.008	±0.005	−0.059	±0.026	±0.021	−0.038	±0.065	±0.047	−0.154	±0.171	±0.050
1410.0	0.910	0.016	±0.009	±0.002	0.014	±0.025	±0.020	−0.036	±0.060	±0.039	−0.400	±0.107	±0.042
1430.0	0.907	0.012	±0.007	±0.004	0.040	±0.021	±0.009	0.179	±0.076	±0.029	0.180	±0.147	±0.043
1450.0	0.903	0.023	±0.007	±0.006	0.100	±0.021	±0.009	−0.011	±0.063	±0.011	0.015	±0.214	±0.032
1470.0	0.900	0.045	±0.008	±0.005	0.028	±0.030	±0.015	0.208	±0.134	±0.025			
1490.0	0.896	−0.011	±0.007	±0.002	0.104	±0.040	±0.030	0.154	±0.121	±0.058			
1510.0	0.892	0.000	±0.008	±0.002	−0.044	±0.030	±0.006	−0.057	±0.110	±0.008			
1530.0	0.887	−0.045	±0.007	±0.004	−0.061	±0.029	±0.003	0.220	±0.141	±0.008			
1550.0	0.883	−0.055	±0.006	±0.002	−0.176	±0.048	±0.017	−0.677	±0.226	±0.023			
1570.0	0.878	−0.070	±0.006	±0.004	−0.035	±0.055	±0.039	−0.162	±0.475	±0.021			
1590.0	0.873	−0.065	±0.006	±0.006	−0.168	±0.053	±0.010	−0.689	±0.156	±0.072			
1610.0	0.868	−0.089	±0.006	±0.004	−0.217	±0.039	±0.011	−0.644	±0.208	±0.022			
1630.0	0.863	−0.072	±0.007	±0.005	−0.315	±0.067	±0.011						
1650.0	0.857	−0.068	±0.008	±0.010	−0.109	±0.086	±0.023						
1670.0	0.852	−0.024	±0.009	±0.010	−0.110	±0.093	±0.020						
1690.0	0.845	0.008	±0.011	±0.005	0.096	±0.118	±0.044						
1710.0	0.839	−0.001	±0.008	±0.002	−0.010	±0.022	±0.029						
1730.0	0.832	0.011	±0.006	±0.001	0.088	±0.071	±0.005						
1750.0	0.826	−0.009	±0.005	±0.003	0.058	±0.045	±0.004						
1770.0	0.818	−0.010	±0.005	±0.002	−0.206	±0.096	±0.020						
1790.0	0.811	−0.027	±0.004	±0.001									
1810.0	0.803	−0.026	±0.005	±0.001									
1830.0	0.795	−0.028	±0.005	±0.002									
1850.0	0.786	−0.034	±0.005	±0.001									
1870.0	0.777	−0.041	±0.005	±0.002									
1890.0	0.768	−0.041	±0.005	±0.001									
1910.0	0.759	−0.033	±0.005	±0.001									
1930.0	0.749	−0.041	±0.006	±0.002									
1950.0	0.738	−0.039	±0.014	±0.002									